

Hydrazine modified g-C₃N₄ with enhanced photocatalytic activity for degradation of indigo carmine

Karen Valencia G^{a,*}, Agileo Hernández-Gordillo^{a,1}, Melissa Méndez-Galván^b, Diego Morett^a, Sandra E. Rodil^a

^a Instituto de Investigaciones en Materiales, Universidad Nacional Autónoma de México, Circuito Exterior SN, Ciudad Universitaria, CP 04510, Coyoacán, Mexico

^b Instituto de Física, Depto. Física Química, Universidad Nacional Autónoma de México, Ciudad Universitaria, CP 04510, Coyoacán, Mexico



ARTICLE INFO

Keywords:
Indigo carmine
g-C₃N₄
Photocatalysis

ABSTRACT

Polymeric graphitic carbon nitride (g-C₃N₄) was obtained from urea and modified by heat polymerization at 550 °C in the presence of hydrazine as a modifier agent. The influence of in-situ generated NH₃ by hydrazine decomposition at different contents (0.5, 1, 1.5, and 2 mL) on the physicochemical properties and surface properties (water contact angle and point of zero charge) of the g-C₃N₄ were investigated. The modified g-C₃N₄ were analyzed by X-ray diffraction, scanning electron microscopy, diffuse reflectance spectroscopy, X-ray photoelectron spectroscopy, photoluminescence, Fourier Transform Infrared, water contact angle, surface area, and the point of zero charge. The in-situ generated NH₃ induced an evolution from nano-flakes to lamellar plate morphology depending on stacked interplanar. The influence of surface properties on the photocatalytic response of the unmodified and modified g-C₃N₄ was tested in the photodegradation of indigo carmine dye at pH = 3.5 and 6.5 solutions under blue LEDs light. The photostability of the samples was tested after 4 cycles of reaction. The properties (surface area (SA); water contact angle (WCA), and optical gap) influence the photocatalytic response, which was summarized in a single parameter defined as SA/(WCA*gap). The maximum value of this product match with results obtained for the most active photocatalyst (U-Hz1).

1. Introduction

Due to the textile and pharmaceutical industry's growth, wastewater containing large amounts of organic dyes are discarded in water effluents, which has become a severe environmental problem worldwide [1,2]. One of the most widely used dyes for denim dyeing and additive in pharmaceutical tablets is indigo carmine (IC), a toxic dye [3–5]. There are various methods for the treatment of dye-contaminated wastewater, such as adsorption [6], anaerobic/aerobic treatment [7,8], and advanced oxidation processes (AOPs) [1,4,9]. Among the AOPs, the photocatalytic process uses light and a semiconductor (the photocatalyst) to promote the degradation of pollutants [10,11]. Diverse inorganic photocatalysts have been studied, such as TiO₂, ZnO, Bi₂O₃, ZnS, etc. [5,11–15]. The disadvantage of most inorganic semiconductors is that they can only be excited using ultraviolet light, which corresponds only to 2–4% of the solar spectrum [16–18]. Therefore, significant efforts have been made to develop photocatalysts capable of

absorbing the visible spectrum [10,19]. Polymeric graphitic carbon nitride (g-C₃N₄), with a narrow bandgap of Eg = 2.7 eV (450 nm) [20], has gained considerable attention due to its availability, non-toxicity, high thermal, and chemical stability [21–24]. The g-C₃N₄ is easily prepared by the thermal polycondensation method using nitrogen-rich precursors including melamine, cyanamide, dicyandiamide, triazine, thiourea, and urea [24–26]. The g-C₃N₄ has been studied as a photocatalyst for water-splitting to reduce CO₂ and decompose various dye contaminants [27–29]. It has been identified that the high electron-hole recombination rate limits the extensive use of g-C₃N₄ [11,19]. On the other hand, another limiting factor is its hydrophobic character which reduces the adsorption of chemical species and affects the photocatalytic property [29–31]. Diverse strategies such as doping with metal/non-metal ions, junction formation with other semiconductor materials, and modifying agents [22,28,32,33] have been applied to improve the photocatalytic activity of g-C₃N₄. One approach to avoid the recombination of electron-hole pairs is to modify the nitrogen

* Corresponding author.

E-mail addresses: karenvalenciag@ciencias.unam.mx, karenvalenciaunam@gmail.com (K. Valencia G), dmorett92@gmail.com (D. Morett).

¹ CONACYT Research Fellow.

content in the tris-triazine rings, which means varying the C/N ratio [34]. The variation of the C/N ratio causes the generation of defect states that can act as electron traps [26,29]. Meanwhile, the hydrophilicity of the material can be increased by the protonation, hydroxylation, or hydroxylamination of the g-C₃N₄ surface [31,35].

Therefore, various modifying agents such as HCl, HNO₃, ethylenediamine, or hydrazine have been tested to improve the photocatalytic response of the g-C₃N₄ under visible light [29,33,36]. For example, Zhang et al. [37] reported the treatment of g-C₃N₄ with HNO₃ in the sol processing of a colloidal suspension (chemical protonation), modifying the optical properties by expanding the absorption range towards the visible spectrum. Kong et al. [38] synthesized g-C₃N₄ nanosheets by polycondensation dispersed in concentrated HNO₃, generating in-plane nitrogen vacancies, where the modified g-C₃N₄ was used to obtain acetone from 2-propanol via photocatalysis. Chen et al. [27] obtained modified g-C₃N₄ by polycondensation using a chemical bath in hydrazine, finding that the diazanyl (NHNH₂) group was successfully introduced onto the g-C₃N₄ surface, which influenced the optical properties, electronic structure, and morphology. Fang et al. [39] obtained nitrogen self-doped g-C₃N₄ via calcining the melamine, followed by a treatment of nitrogen-rich additive (hydrazine). As a result, the modified g-C₃N₄ showed superior photocatalytic hydrogen evolution, 1.8 times higher than pristine g-C₃N₄. A higher optical absorption explained the improvement. Shi et al. [40] synthesized g-C₃N₄ by heating dicyandiamide at 550 °C, followed by a photo-assisted treatment with hydrazine in a batch-type reaction. Such process generates nitrogen vacancies in the tri-s-triazine units of g-C₃N₄, inducing defect states that extend the bandgap to the visible-light absorption range and suppress the radiative electron-hole recombination. The modified g-C₃N₄ photocatalysts show much higher photocatalytic activity for H₂O₂ production with optimized enhancement up to ten times higher than pristine bulk g-C₃N₄.

In all these examples, the distortion and C/N ratio variation in the g-C₃N₄ structure were essential in modifying the physicochemical properties and improving the photocatalytic response using external processes. However, the role of the material's wettability on the photocatalytic response has not been thoroughly evaluated [41,42]. In this article, modified g-C₃N₄ was synthesized by polycondensation using urea as the precursor in the presence of hydrazine as an *in-situ* modifier agent. The effect of the hydrazine content on the optical absorption, the hydrophobicity/hydrophilicity properties, and the photocatalytic activity was evaluated. The photocatalytic activity was examined by monitoring the degradation of the IC dye under blue light irradiation. A correlation between the different physicochemical parameters and the IC dye degradation is proposed.

2. Experimental details

2.1. Synthesis of modified g-C₃N₄

The modified g-C₃N₄ were prepared using urea (CO(NH₂)₂, JT Baker 99.5%) as the precursor by heat polymerization in the presence of hydrazine (N₂H₄, Sigma Aldrich 25% vol.) as the *in-situ* modifier agent. The process consisted of melting 5 g of urea for 30 min, and then the melted urea was mixed with a certain amount of hydrazine (0.5, 1, 1.5, and 2 mL). The mix was placed in a ceramic-covered crucible and annealed at 550 °C temperature (5 °C/min ramp) in static air for 2 h. The obtained polymerized samples were labeled as U-HzX, where X represents the amount of hydrazine in mL. Additionally, an unmodified g-C₃N₄ sample was obtained without hydrazine, and it was labeled simply as U.

2.2. Characterization of modified g-C₃N₄

The as-prepared materials were characterized by X-ray diffraction (XRD) using a Siemens D500 diffractometer using the Cu K α radiation of 0.15406 nm (34 kV, 25 mA) and a scanning range between 5 and 60° (2

theta) with a step size of 0.013°/s. The morphology of the samples was analyzed by Scanning Electron Microscopy (SEM) using a JEOL 7600 F at 10 kV. The specific surface area of the material was determined by the BET method from the nitrogen adsorption-desorption isotherms at 77.4 K. The analysis was made using a Quantachrome Autosorb instrument. Before the measurements, the powered samples were degassed at 200 °C in a vacuum for 12 h.

The UV-vis diffuse reflectance spectra (DRS) were obtained on a Shimadzu 2600 equipped with an integration sphere ISR 2600 in the interval from 190 to 700 nm BaSO₄ was used as a reference blank. The absorbance spectra were obtained, and the bandgap energy (E_g) was calculated using the Kubelka-Munk model, considering an indirect transition for g-C₃N₄ material [11] by extrapolating the linear portion of the $(F(R) \propto h\nu)^{\frac{1}{2}}$ versus $h\nu$ curves to $F(R)$. The chemical composition of the as-prepared materials was evaluated by X-ray photoelectron spectroscopy (XPS) using the XPS microprobe PHI 5000 Versa Probe II of Physical Electronics. A monochromated Al K α ($h\nu = 1486.6$ eV) X-ray source was used at 25 W with 100 μm of the beam diameter. The surface of each sample was etched for 5 min with 1 kV Ar + at 500 nA current with a significant modification of the spectra, indicating that the adsorbed carbonaceous species were effectively removed. The XPS spectra were acquired at 45° from the surface in constant pass energy mode (CAE) at $E_0 = 117.40$ and 117.75 eV for the survey and high-resolution spectra. The C1s signal at 284.8 eV was used to correct the binding energies. The photoluminescence, PL spectra were recorded using an Edinburgh instrument FS5 fluorimeter with a 150 W, CW ozone-free xenon arc lamp. The FTIR absorption spectra were recorded on a Thermoscientific Nicolet 6700 spectrometer provided with an ATR accessory and a diamond crystal. The pressure used was 815 Psi at room temperature, 68 scans at a resolution of 4 cm⁻¹ in the interval from 500 to 3600 cm⁻¹ in the transmittance mode.

The water contact angle (WCA) was tested by OCA 15 EC (Dataphysics) goniometer via the static sessile drop method, the water droplet was about 3 μL, and the equilibrium time was 40 s. The point of zero charge (PZC) was measured using a modified batch equilibrium method. The suspension was prepared by dispersing 5 mg of the modified g-C₃N₄ in 6 mL of distilled water, previously adjusting the pH values at 2.7, 4.8, and 6.3 by drop to drop of CH₃COOH (JT Baker, 99.8%) solution. Then it was left in equilibrium for 72 h, and the final pH (pH_f) was registered using a 3540 pH Tester (JENWAY). The difference between the initial pH (pH_i) and final pH (pH_f-pH_i) was plotted against pH_i, and the point where pH_f-pH_i = 0 was taken as the PZC of each sample according to the reported methodology [43,44].

2.3. Photocatalytic test of modified g-C₃N₄

The photocatalytic activity of the modified g-C₃N₄ was evaluated using 10 mg of photocatalyst powder through 200 mL (0.05 mg/L) of an aqueous solution at 5 ppm of IC dye at natural pH (~ 6.5), stirred at 1000 RPM at room temperature in an open air-glass reactor system. Before irradiation, the suspension was kept under dark conditions for 30 min (adsorption-desorption equilibrium); subsequently, it was irradiated for about 80 min using a light array, which consisted of 9 blue LED lamps of 3 W (maximum emission light at $\lambda = 455$ nm) placed around the glass reactor at a distance of 1 cm. The IC dye concentration was quantified following the absorption band at 610 nm, analyzing the filtered aliquot of 3 ml at different time intervals using UV-vis spectroscopy (Shimadzu 1800 spectrometer). The apparent kinetic reaction was estimated by using the Langmuir Hinshelwood kinetic model of pseudo-zero order, which is expressed as $\frac{C}{C_0} = 1 - \frac{k_{app}t}{C_0}$, where the slope is the apparent kinetic rate constant (K_{app}), divided by the initial concentration ($\frac{k_{app}}{C_0}$) [45].

Additional photocatalytic test for all the modified g-C₃N₄ was performed at two pH solutions: natural pH (~ 6.5) and at pH of ~ 3.5 adjusted with CH₃COOH solution, following the same methodology

mentioned above. The photostability of the best sample was evaluated by measuring XRD and FTIR after 4th cycles of reaction using the same photocatalytic conditions.

3. Results and discussion

3.1. Crystalline structures of g-C₃N₄

Fig. 1-a, shows the XRD patterns of the unmodified and modified g-C₃N₄ samples prepared in the absence (U) and the presence of hydrazine (U-HzX), respectively. All the polymerized samples exhibit two broad diffraction peaks at about $\sim 13^\circ$ and $\sim 27^\circ$ in 2 θ , corresponding to the (100) and (002) diffraction planes, respectively, which are associated with the tetragonal phase of g-C₃N₄ (JCPDS 87-1526) [46,47]. The (100) crystal plane is attributed to the interlayer structural unit (triazine rings), and the (002) signal can be associated with the interplanar stacking along the c-axis of the graphite-like materials [41,48,49]. For

the modified g-C₃N₄ samples, polymerized in the presence of high hydrazine content, the peak at 27° in 2 θ is more intense, which suggests that the interplanar stacking of g-C₃N₄ increases as a function of the hydrazine content [50–52]. These results suggest that increasing the amount of hydrazine during the polymerization process promotes the stacking of the graphitic layers (see **Fig. 1-b**).

3.2. Morphology and textural properties of g-C₃N₄

The variations in the morphology of the modified g-C₃N₄ samples are shown in **Fig. 2** for low (U, U-Hz0.5, and U-Hz1) and high (U-Hz1.5 and U-Hz2) hydrazine contents. The unmodified U sample exhibits a nano-flake morphology with dimensions of ~ 10 nm of thickness and length of ~ 0.3 – 0.7 μm . Typically flake morphologies are obtained in ammonia (NH₃) poor atmospheres when urea is used as the unique precursor, although larger (~ 2 – 10 μm) [29,30,37]. The morphology changed to porous and lamellar plates, adding low hydrazine content, U-Hz0.5, and

FIGURE CAPTIONS

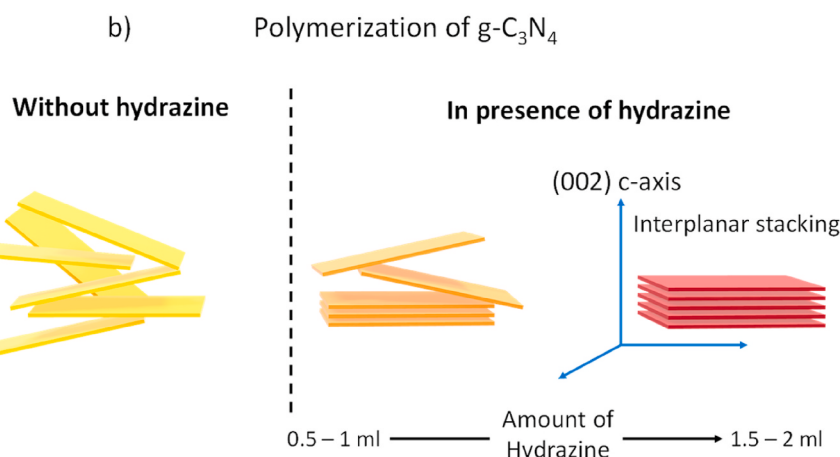
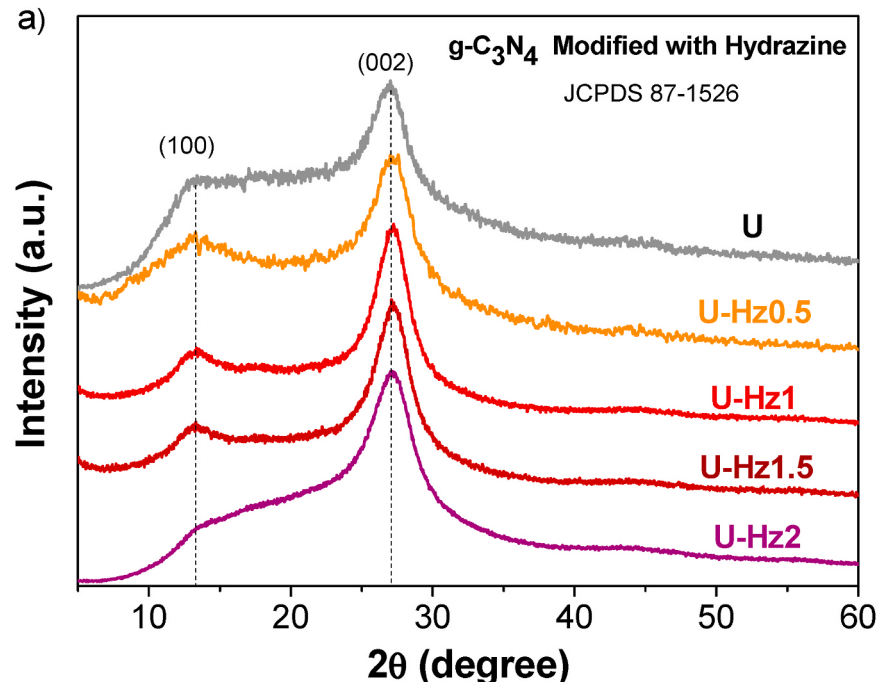


Fig. 1. a) X-ray diffraction patterns of unmodified and modified g-C₃N₄, and b) Schematic representation the stacking of interlayers of g-C₃N₄ along the c-axis, prepared in the presence of different hydrazine contents.

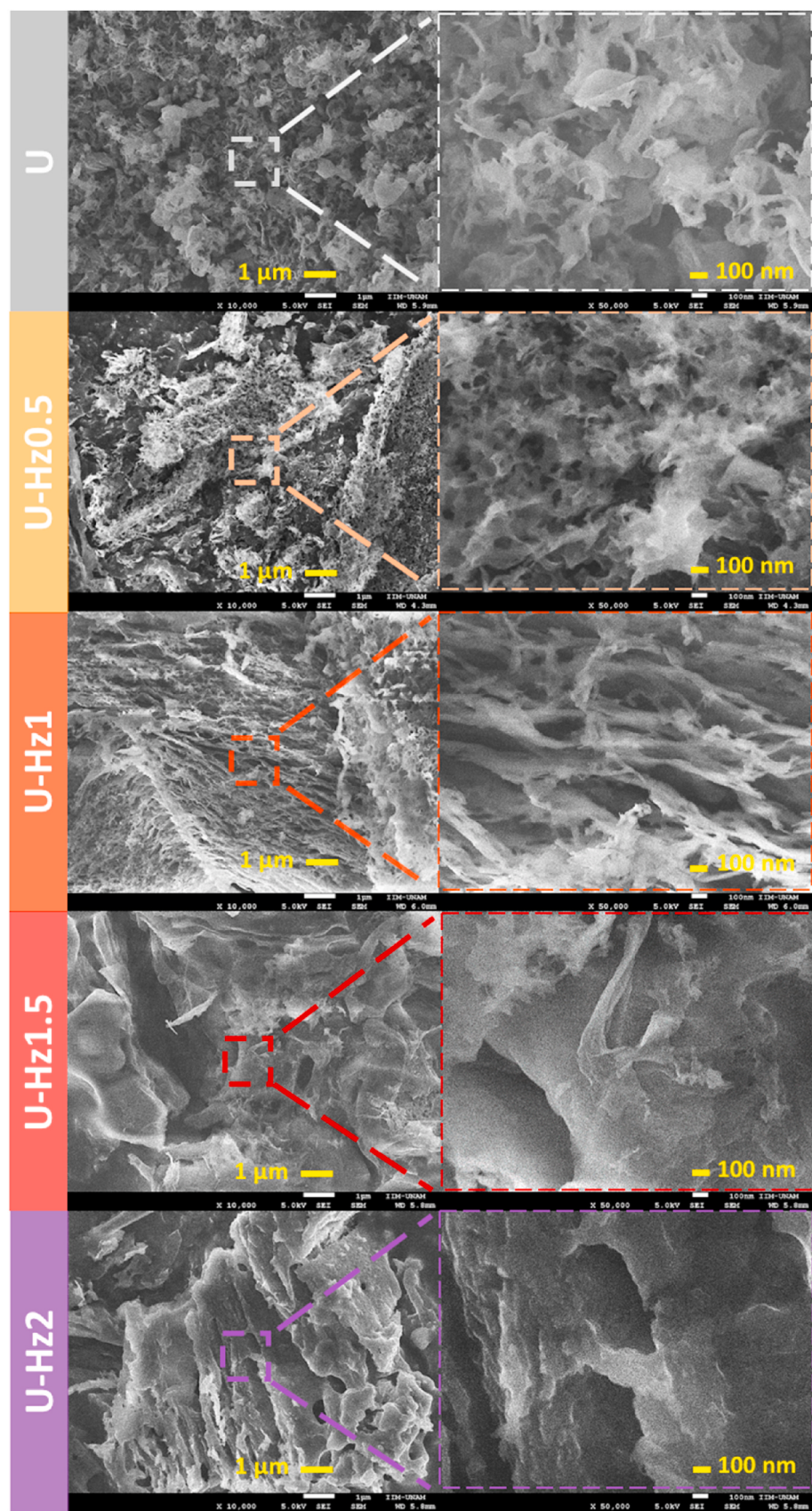


Fig. 2. SEM image of unmodified (U) and modified $\text{g-C}_3\text{N}_4$ (U-Hz0.5, U-Hz1, U-Hz1.5 and U-Hz2 samples), prepared in the presence of: 0, 0.5, 1, 1.5 and 2 mL of hydrazine.

U-Hz1 samples. Larger quantities of hydrazine (1.5–2 mL) led to a plate-morphology presenting a compacted structure of large dimensions: ~5–10 μm long and 250 nm thickness. The hydrazine addition increases the ordered stacking of the triazine layers obtaining more compact structures at large quantities of hydrazine, which impacts the SA of the materials. The textural properties of the modified g-C₃N₄ samples were studied by N₂ adsorption-desorption isotherms (Figure A1). The samples exhibit isotherm curve characteristics of type IV with the H3 hysteresis loop. This type of hysteresis is typically observed in mesoporous materials with slit-shaped pores [53]. The estimated specific surface area (SA) decreases due to the hydrazine contents. So, from Table 1, it can be observed that the unmodified U sample presents the highest value of SA (56 m²/g), which is close to that reported in the literature when the g-C₃N₄ is polymerized from urea precursor at similar annealing conditions [29,54–56]. By contrast, for the modified g-C₃N₄ samples, the SA decreases 3.3 times that of the U sample, obtaining a minimum value of 17 m²/g for the U-Hz2 sample. Such decrement agrees with the observed compact structure seen for the U-Hz2 sample by the SEM.

The observed change from nano-flakes to a compact morphology as the hydrazine content increased could be explained by the presence of NH₃ generated by the thermal decomposition reaction of both urea and hydrazine [57–59]. Around 200 °C, the hydrazine is decomposed into NH₃, N₂, and H₂, generating an ammonia-rich atmosphere by the following reactions [57,59]:



It was reported that a high fraction of NH₃ released during the polycondensation process led to the formation of sheets of g-C₃N₄ slightly rolled, forming porous plates [26,60,61]. Similar small g-C₃N₄ rolled flakes were obtained by I. Papailias et al. [26] using melamine as the precursor and different annealing temperatures. The possible cause of these rolled structures is that large amounts of NH₃ flow vertically through the melamine layers, forming rolled-out sheets to reduce the surface energy, as observed by other authors [60,61]. We suspect that a parallel effect occurs in the g-C₃N₄ materials synthesized with a high hydrazine content, where the NH₃ production is also increased during the polymerization process. The gaseous NH₃ must flow to the upper part of the close reactor and, in the process, induce the ordering of the growing C₃N₄ laminar structures, which at large hydrazine content look like compact structures (Figs. 2 and 3).

3.3. Optical properties

The DRS of the g-C₃N₄ samples are shown in Fig. 3. For the nano-flake U sample, the absorbance edge starts at ~500 nm with maximum absorption at ~370 nm, indicating absorption in the UV light region, corresponding to the electronic transition from the valence band to the conduction band of the g-C₃N₄ [29,30,62,63]. At around ~370 nm, a maximum absorption was also observed for nano-flake U-Hz0.5 and U-Hz1 samples. However, a broad shoulder begins to grow at about ~475 nm until ~650 nm. This behavior is more evident in the compacted porous structure of U-Hz1.5 and U-Hz2 samples than in the nano-flakes, where the visible absorption is extended until ~700 nm. The obtained visible absorption spectrum is according to the samples' observed color, from pale yellow for the U sample to a red-wine for the U-Hz2 sample (powder photo in Fig. 3). This result suggests that the

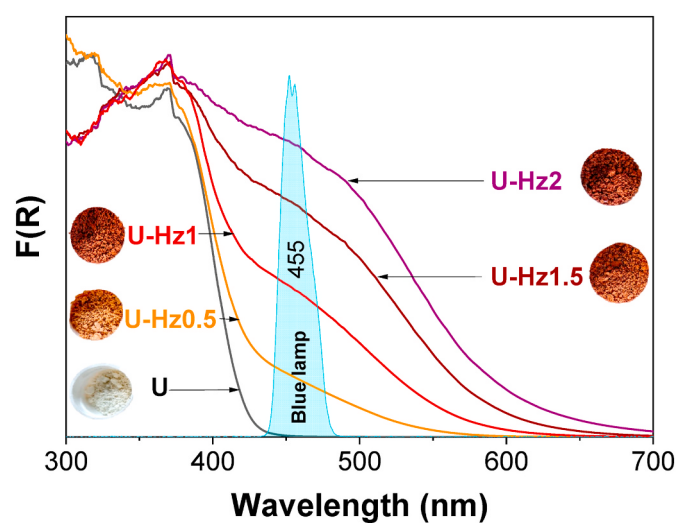


Fig. 3. UV-vis DRS spectra and powder photo the unmodified and modified g-C₃N₄ samples prepared in the presence of different hydrazine contents. As well as the spectrum of the blue LED lamp.

absorption spectrum of modified g-C₃N₄ samples widened towards the visible spectrum, which could be related to structural defects in the interlayer of g-C₃N₄ due to N vacancies [63,64].

All the samples' bandgaps were determined using the Kubelka-Munk function considering indirect band transitions (Figure A2) [22,23,26]. The bandgap for the g-C₃N₄ (U) was 2.8 eV, in agreement with other authors [20,21,41,47,48,65], whereas for modified g-C₃N₄, the bandgap decreases proportionally as the interplanar stacking of the g-C₃N₄ layers increased during the polymerization, obtaining 2.1, 2.0, 1.9 and 1.8 eV for U-Hz0.5, U-Hz1, U-Hz1.5, and U-Hz2 sample, respectively. Fig. 3 includes the blue LED-lamp's emission spectrum to show that all modified g-C₃N₄ can absorb the blue light. The absorption in the visible light region is significant for photocatalytic applications since it can take advantage of the most extensive visible spectrum.

3.4. XPS analysis

The XPS was used to analyze the surface chemical composition and bonding structure for the unmodified and modified g-C₃N₄ samples (U, U-Hz0.5, U-Hz1, U-Hz1.5, and U-Hz2 in Fig. 4-a and 4-b). The samples were sputter-cleaned before the XPS analysis to avoid adventitious carbon's appearance and obtain a better emission corresponding to C1s and N1s bands. From Fig. 4-a, the g-C₃N₄ samples displayed C1s emissions where they were deconvoluted into four peaks. The first peak at ~284.6 eV corresponds to the C-H bonds [66,67], where the amount of C-H was 26.7, 39.2, and 32% for U, U-Hz1, and U-Hz2 samples, respectively. The signal at ~288.2 eV corresponds to the sp²-bonded carbon in the nitrogenous aromatic ring (N=C-N) [18,26,29,68], which is characteristic of g-C₃N₄ material, presenting typically 50.2% of the N=C-N for the unmodified nano-flake U sample. For the modified g-C₃N₄ material, the N=C-N proportion decreased significantly to 38.87 and 44.7% for U-Hz1 and U-Hz2 samples, respectively. The peak centered at 286.3 eV corresponds to C-N₂ [69], with a similar fraction (18.9–21.43%) among the samples. Finally, the additional peak at 293.5 eV is due to excited electrons in the π* orbital of the heptazine units [70].

Fig. 4-b displayed the N1s emissions, that was deconvoluted into four components. The sp² C-NH₂ bonds at 398.5 eV varied randomly from 32.7, 42.5, and 21.3% for U, U-Hz1, and U-Hz2 samples, respectively. The signal at 399.1 eV is due to C-N sp² bonds of the triazine ring structure [71]. The most significant percentage of C-N bonds is observed for the U sample (54.24%), while for the U-Hz1 and U-Hz2 samples was 33.2 and 50.6%, respectively. The peak at 400.9 eV was attributed to

Table 1

Specific surface area of the unmodified and modified g-C₃N₄ samples.

| Material | Specific area (m ² /g) | Diameter Pore Size (Å) |
|----------|-----------------------------------|------------------------|
| U | 56 | 19 |
| U-Hz0.5 | 51 | 20 |
| U-Hz1 | 39 | 37 |
| U-Hz1.5 | 31 | 34 |
| U-Hz2 | 17 | 9 |

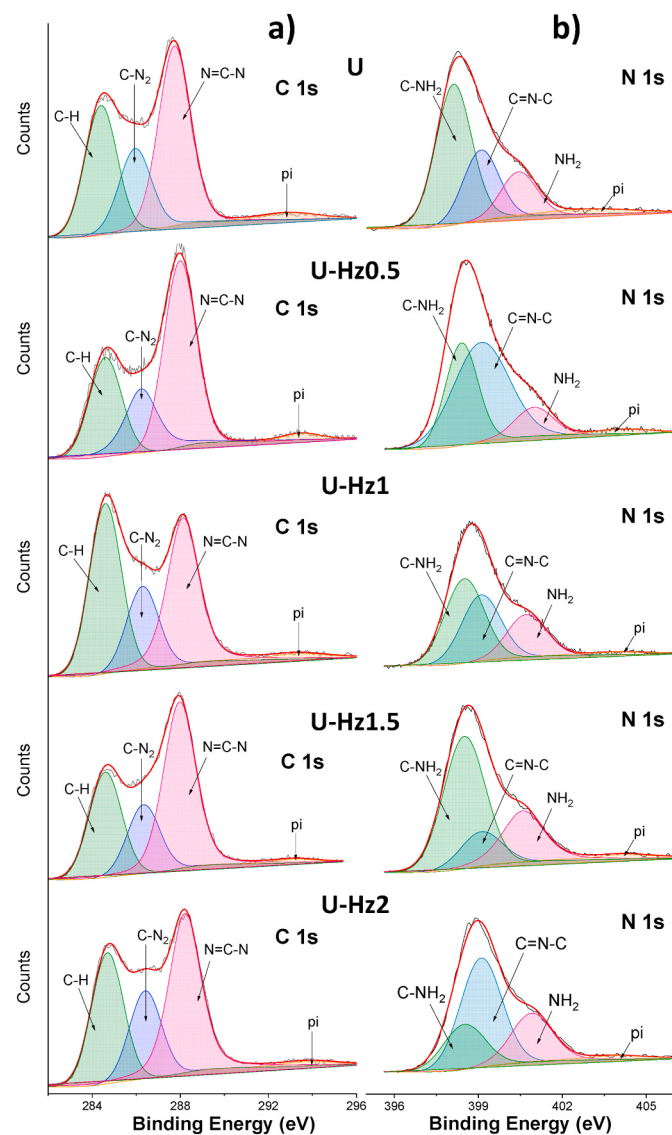


Fig. 4. XPS spectra of a) C 1s and b) N 1s for the unmodified (U) and modified g-C₃N₄ (U-Hz0.5, U-Hz1, U-Hz1.5 and U-Hz2 samples).

H-N-(C)₃ [70], where the lowest amount is observed for the U sample with 10.7%, while for the U-Hz1 and U-Hz2 samples, a similar fraction (21.4 and 24.2%) was observed. Finally, the N1s emissions also displayed a weak feature at 404 eV, usually assigned to excited π^* orbitals as for carbon [29,68,70]. Significant differences were observed in the fraction associated with each bonding, but not a clear trend can be proposed.

The estimated C/N ratios based on the integrated areas under the fitted peaks of the XPS analysis follow the order U-Hz1 > U-Hz2 > U-Hz1.5 > U-Hz0.5 > U, see Table 2. The C/N ratio for the U and U-Hz0.5 samples agrees with the reported theoretical value (0.75) for g-C₃N₄

[26], but for the other samples (U-Hz1 > U-Hz2 > U-Hz1.5), the ratio is larger than the estimated theoretical value, which suggests a trend that the amount of nitrogen decreased with the addition of hydrazine. It suggests that the aromatic carbon-nitrogen rings possibly were not saturated, suggesting the generation of nitrogen vacancies, as has been reported by other authors [63,72]. Nitrogen vacancies can explain the decrease in the band-gap, and the shift in the absorption edge towards the visible region, as shown in Fig. 3 for this modified g-C₃N₄.

3.5. Photoluminescence study

The effect of the hydrazine during the C₃N₄ polymerization on the generation of N vacancies was evaluated using the photoluminescence spectra. Fig. 5a shows the steady-state PL spectra of the unmodified and modified g-C₃N₄ materials measured under optical excitation energy of 3.35 eV, above the bandgap of the samples. At this energy, the diffuse reflectance spectra were similar for all materials, suggesting similar absorption. As the hydrazine increased, the PL maximum exhibited a red-shifting and a decrease in the emission intensity. The following figures (Fig. 5 b–f) show the deconvolution of the PL spectra for each sample. The PL spectrum has a maximum emission in the blue region (at 2.59 eV) with a low-energy tail extending down to 1.6 eV for the U sample. The characteristic blue emission for unmodified C₃N₄ materials is attributed to excitons generated in the s-heptazine ring [73]. As the hydrazine content increases, the maximum emission is red-shifted by ~0.27, 0.47, 0.56, and 0.59 eV for U-Hz0.5, U-Hz1, U-Hz1.5, and U-Hz2 sample, respectively. The observed red-shift spectral could be attributed to structural changes in g-C₃N₄ as it grows due to the possible generation of N vacancies, as suggested by the XPS (Fig. 4), caused by the presence of NH₃ during the synthesis [73,74].

In addition, there is a monotonic decrease in the emission intensity that is ~6.9, 14.6, 25.0, and 34.5 times lower than for the U sample, as hydrazine content increased. This quenching of the emission, together with the red-shift in the PL emission observed for the modified g-C₃N₄ can be attributed to the inhibition of radiative recombination of photogenerated electrons and holes [73,75], which is suggested to promote a better separation of the photogenerated carriers caused by the trapping of charge carriers by states defect.

The unmodified g-C₃N₄ (U) present three Gaussian peaks centered at 2.77, 2.59, and 2.36 eV (Fig. 5b). The three radiative emission bands correspond to transitions from δ^* and π^* in the conduction band to the lone pair state of the bridge N atom in the valence band and π^* to π transitions in the conduction band [73–75].

The modified g-C₃N₄ (U-Hz0.5 and U-Hz1) materials exhibit nearly the same three emission bands as the U-sample, placed at 2.77, 2.57, and 2.28 eV. However, the U-Hz1 shows an additional strong band centered at 2.04 eV, associated with defects states, as N vacancy [73,75,76]. The U-Hz1.5 and U-Hz2 samples exhibit only two emission bands at 2.77 eV, of low intensity, and at 2.04 eV, the larger emission. The possible generation of N vacancies suggested by PL emission is according to the high C/N ratio in U-Hz1.5 and U-Hz2 samples.

3.6. Surface analysis by FT-IR spectroscopy, WCA and PZC

In Fig. 6, the FTIR spectra of modified g-C₃N₄ samples show that the

Table 2
C1s, N1s and C/N ratio for the unmodified and modified g-C₃N₄ samples.

| Sample | C1s [%] | | | N1s [%] | | | C/N ratio |
|---------|--------------|----------------|----------------|----------------------------|----------------|--------------------------|-----------|
| | C-H 284.6 eV | -C-N2 286.3 eV | N=C-N 288.2 eV | C-NH ₂ 398.5 eV | C=N-C 399.1 eV | NH ₂ 400.9 eV | |
| U | 26.7 | 21.12 | 50.22 | 32.37 | 54.24 | 10.68 | 0.71 |
| U-Hz0.5 | 28.91 | 18.9 | 50.45 | 55.84 | 14.48 | 25.62 | 0.73 |
| U-Hz1 | 39.19 | 18.96 | 38.87 | 42.49 | 33.16 | 21.38 | 1.1 |
| U-Hz1.5 | 31.18 | 20.69 | 45.18 | 53.68 | 25.58 | 16.32 | 0.83 |
| U-Hz2 | 32.01 | 21.43 | 44.75 | 21.32 | 50.57 | 24.19 | 0.9 |

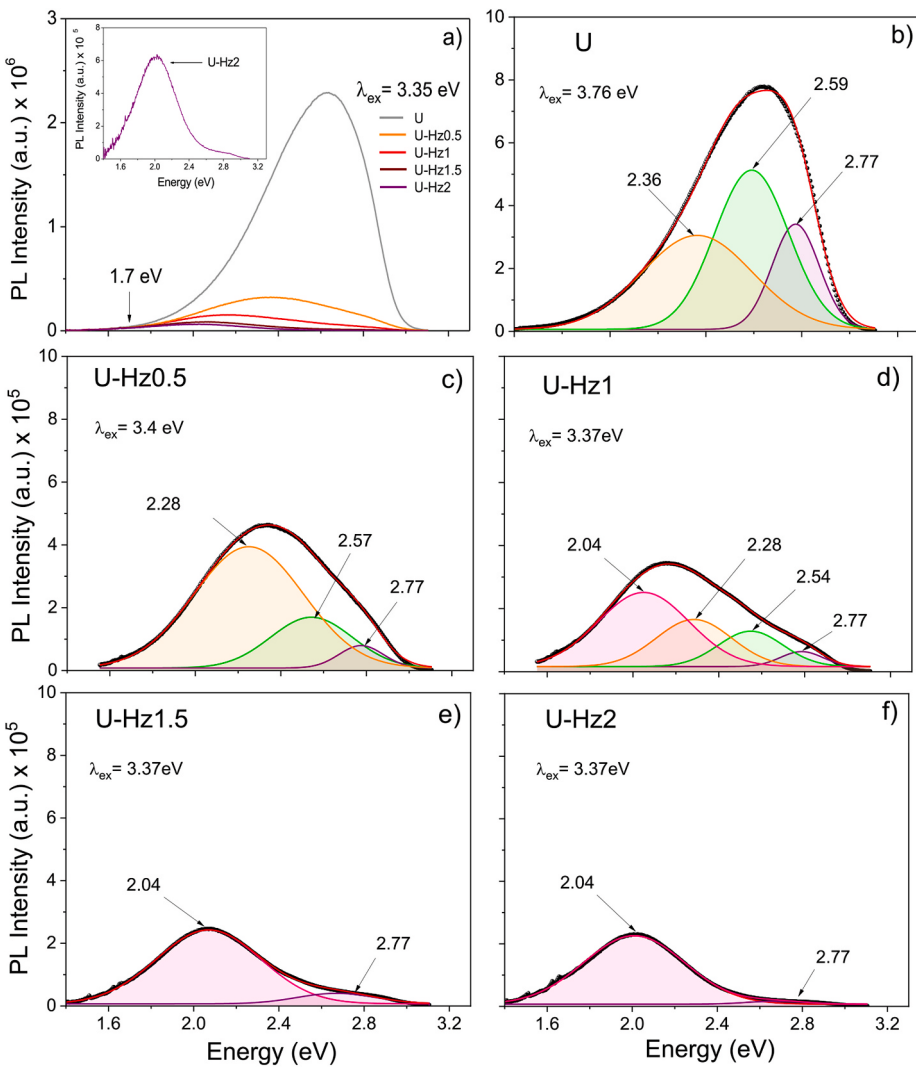


Fig. 5. a) PL spectra of unmodified and modified g-C₃N₄ under excitation energy of 3.35 eV, above the bandgap of the samples. The inset shows a magnified view of the PL spectrum of U-Hz2. (b–f) Deconvoluted (Gaussian) PL spectra of unmodified and modified g-C₃N₄ samples obtained under different excitation energies.

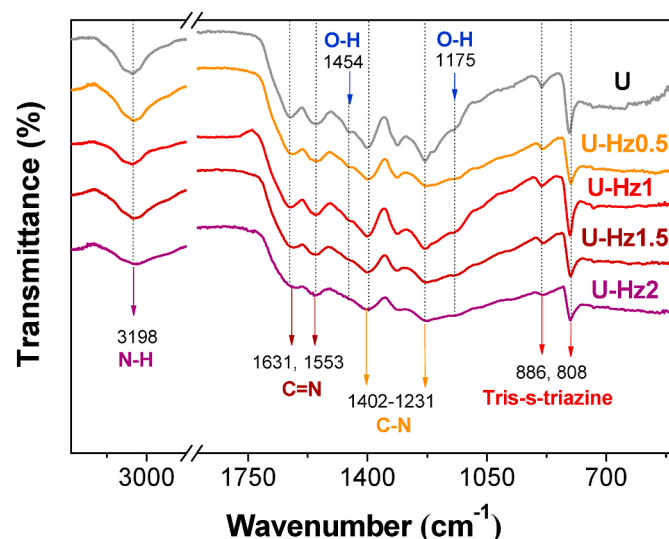


Fig. 6. FTIR of the unmodified and modified g-C₃N₄ prepared in the presence of different hydrazine contents.

bonding structure was similar between all samples. Broad peaks at 3198 cm⁻¹ belong to the stretching vibrations of N-H in the terminal amine groups [37]. The absorption bands at 808 and 886 cm⁻¹ are characteristic of the tris-s-triazine bending modes [42,50]. The stretching vibrations of aromatic C–N heterocycles are observed at 1231, 1314, and 1402 cm⁻¹ [18], while the peaks at 1553 and 1631 cm⁻¹ are attributed to the C≡N stretching vibrations [37,50]. The absorption peaks at 3452, 1454, and 1175 cm⁻¹ are related to the presence of –OH groups, but it is challenging to determine the OH proportions due to overlapping with other bands. In this line, it is known that the topographic and the chemical composition of the surface, like hydroxyl groups, improve the materials' hydrophilicity and the surface interaction with water molecules in polar media [77–79]. Therefore, WCA measurements were done, and the results are shown in Fig. 7. The WCA value increase following the U-Hz1 < U-Hz0.5 < U < U-Hz1.5 < U-Hz2 order, observing that the U-Hz1 sample presents the smallest WCA. Considering that surfaces are hydrophobic when the WCA is > 90° and hydrophilic when WCA is < 90°, none of the samples are purely hydrophobic. However, the U-Hz1 is the most hydrophilic sample that must be a balance between the surface roughness and the presence of –OH groups observed by FT-IR (Fig. 6).

On the other hand, the PZC refers to the pH at which the electrical charge density on the surface semiconductor (g-C₃N₄) is equal to zero [80]. Using the modified batch equilibrium method, the PZC value of the

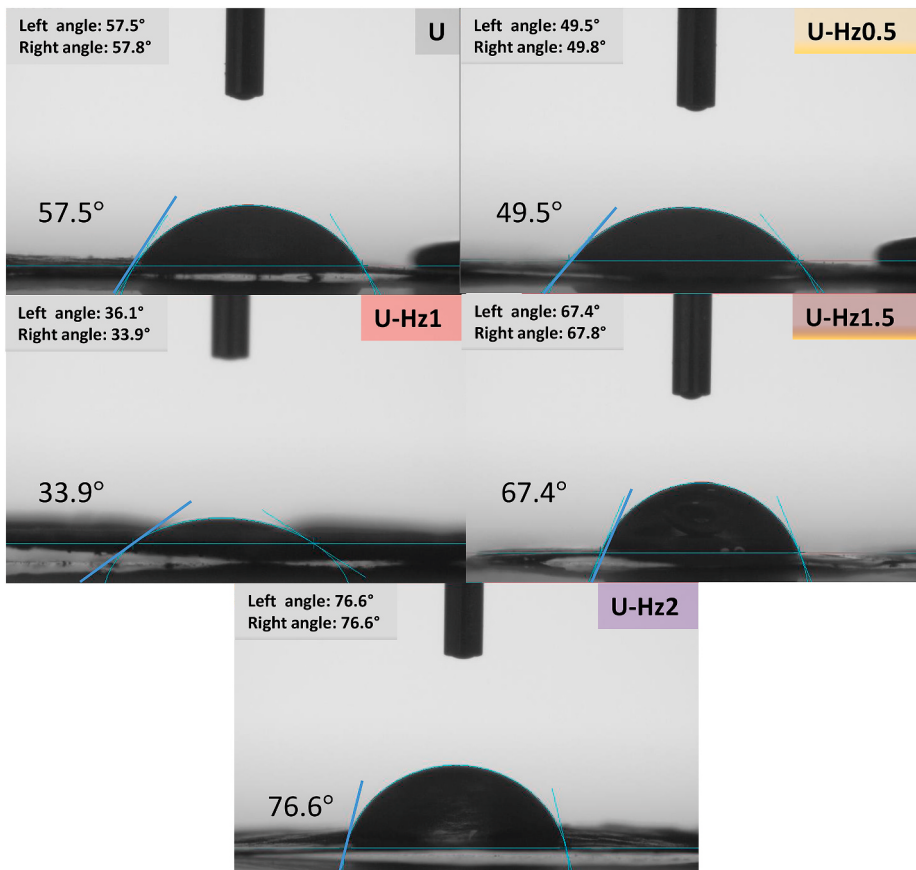


Fig. 7. Water contact angle (WCA) measurements of a water droplet on the unmodified and modified $\text{g-C}_3\text{N}_4$ prepared in the presence of different hydrazine contents.

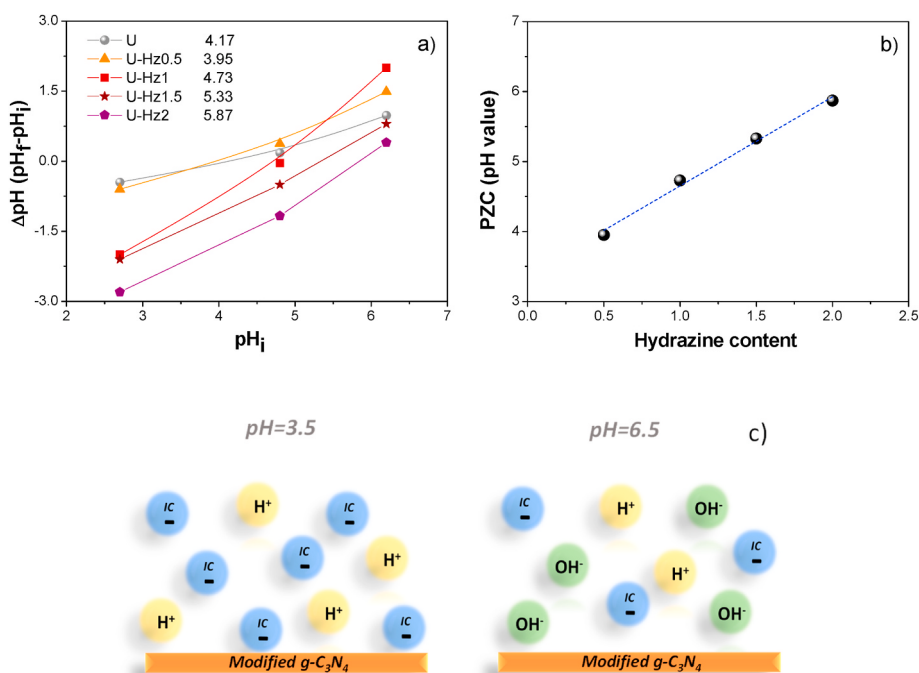


Fig. 8. a) Point of zero charge (PZC) for unmodified and modified $\text{g-C}_3\text{N}_4$, b) linear behavior of PZC as a function of the hydrazine content, and c) Schematic representation of the interaction of ionic species in solution on the photocatalysts surface at $pH = 3.5$ and 6.5 .

U sample was 4.17 (Fig. 8-a), which agrees with the reported value [24, 81]. For modified g-C₃N₄ samples, the PZC value increased linearly as the NH₃ contents were raised, directly associated with hydrazine content (Fig. 8-b). The PZC value is an important surface property because it directly affects anionic or cationic molecules' adsorption capacity in the aqueous solution [24, 82]. When the pH of the solution is below the PZC value of the sample, the semiconductor surface becomes positively charged (H⁺); therefore, the surface favors the electrostatic adsorption of negatively charged pollutants. While for PZC < pH of the solution, the adsorption of positively charged contaminants is favored (Fig. 8-c). The PZC values were between 3.95 and 5.87, therefore the photocatalytic evaluation at ~3.5 and ~6.5 pH solutions were done to investigate the role of electrostatic controlled adsorption. The anionic character of the IC dye molecule suggests that adsorption should be favored at 3.5, where the unmodified or modified g-C₃N₄ surfaces are positively charged. Therefore, even the less hydrophilic samples could absorb anionic molecules at pHs < 5. Similar behavior was observed by Bicheng Zhu et al. [83], when g-C₃N₄ was synthesized by heating melamine, thiourea, and urea directly. The prepared samples showed different microstructures and PZC values that affect their adsorption capacity. The PZC values of the g-C₃N₄ samples were between 4 and 5. Consequently, the adsorption of methyl orange, which is an anionic dye, did not show significant variations. Meanwhile, the concentration of methylene blue, which is a cationic dye, decreases drastically in a very short time.

3.7. Photocatalytic performance

The dye adsorption capacity and photocatalytic activity of all the g-C₃N₄ samples were evaluated for the photodegradation of 5 ppm of IC dye under blue irradiation at pH = ~3.5 and ~6.5. The two pH values were selected to distinguish the interplay between wettability and PZC (adsorption capacity). The absorbance spectrum of the IC dye solution owed to the indigoid group was unaltered when the photolysis reaction was carried out under blue light during 4 h of reaction (not shown). Fig. 9 and Figure A3 show representative absorbance spectra of the IC solution for all the as-prepared samples at the two pH values as a function of the illumination time. For the U sample, the IC dye was slightly degraded; the absorbance remained nearly unchanged after 80 min of illumination at both pH values.

Meanwhile, for the U-Hz1 sample, the absorbance bands of the IC dye at 610 and 287 nm decreased as the irradiation time progressed (Fig. 9); the reduction was more significant at a pH of 6.5. It suggests that the IC dye was degraded using the modified g-C₃N₄ by the photocatalytic process. Moreover, the decrease in the color bands (610 and 287 nm) was accompanied by an increase in a secondary band at 243 nm, generating an isosbestic point at 251 nm (Fig. 9). Analyzing the simulated theoretical spectra of IC, isatin sulfonic acid, and 2-amino-5-sulfobenzoic acid, computed with TD-DFT, reported by A. Hernández-Gordillo et al. [84], the presence of an isosbestic point around 251 nm suggests the presence of both isatin sulfonic acid and

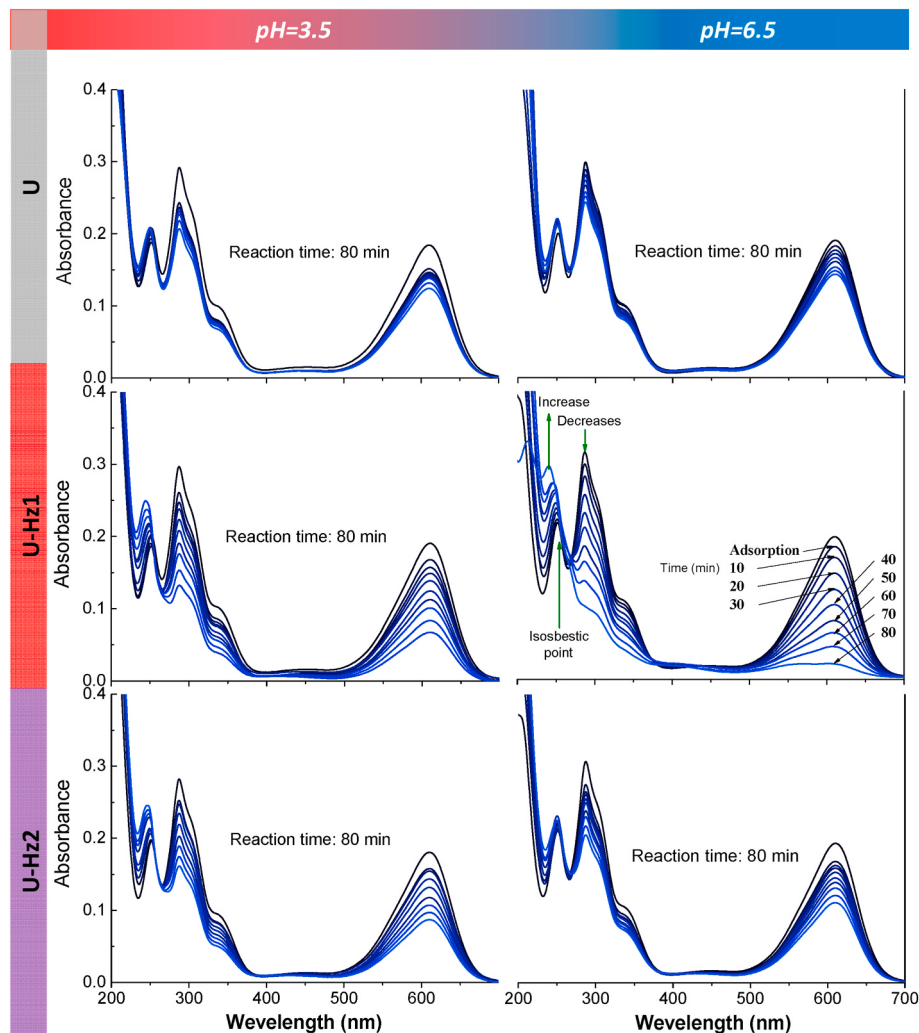


Fig. 9. Absorbance spectra of 5 ppm of IC dye degradation as a function of blue light irradiation time, using 0.05 mg/L of U, U-Hz1, and U-Hz2 powder at pH = 3.5 and 6.5.

2-amino-5-sulfobenzoic acid intermediates. These absorbance peaks and the formation of both intermediates have been observed by other authors [84–87]. The new absorption bands and isosbestic point observed during the degradation experiments suggest that the IC dye was possibly degraded into isatin sulfonic acid and 2-amino-5-sulfobenzoic acid as intermediate products after the photocatalytic process using g-C₃N₄ as photocatalyst material.

Fig. 10-a and **10-b** show the IC dye's relative concentration profile (C/C_0) versus time at the two pHs, ~ 3.5 and ~ 6.5 , respectively. It can be seen that at pH = ~ 6.5 (**Fig. 10-b**), the unmodified g-C₃N₄ (U) was the least photoactive material, reaching a degradation percent of 27% in 80 min, while the most active material was the modified U-Hz1, presenting 86% of IC degradation at the same time. A similar trend was observed at pH = ~ 3.5 , where the most active material is U-Hz1 (see **Fig. 10-a**). Assuming a zero-order reaction (where the kinetic rate constant is independent of reactant concentration), the apparent kinetic rate constants (K_{app}) were obtained at the two pHs (**Fig. 11-a** and **11-b**). **Fig. 11-b** summarizes the adsorption percentage together with the K_{app} value at pH = ~ 6.5 for all the samples, between 1.4 and 5.2×10^{-2} ppm min⁻¹. It is observed that the unmodified U material is the least active in the degradation of the IC dye, presenting a K_{app} of 1.4×10^{-2} ppm min⁻¹, despite being the material with the larger SA. The low activity can be explained because of the low capacity to absorb blue light. For the modified U-Hz0.5 and U-Hz1 materials, the photoactivity increases reaching a K_{app} of 3.9 and 5.2×10^{-2} ppm min⁻¹, respectively, representing 3.5 times with respect to U material. The high photoactivity could be related to diverse factors a) high capacity to absorb blue light, b) the presence of surface defects, and c) the more hydrophilic nature.

Additionally, the polymerization of g-C₃N₄ in high hydrazine contents led to a decrease in the activity (U-Hz1.5 > U-Hz2). Although both samples can absorb blue light and have surface defects and adequate PZC to absorb the more anionic IC dye, the detriment in photoactivity appears to be related to the low hydrophilicity. The more significant degradation rate was obtained for the samples with the lowest WCA (U-Hz1), confirming that the hydrophilicity parameter directly affects the interactions of materials surface with the adsorbed pollutants, which is interpreted to affect the photocatalytic activity's behavior.

3.8. Stability study of the U-Hz1 photocatalyst

Stability studies were performed using the most active photocatalyst (U-Hz1), tested during 4 cycles of reaction at 80 min of irradiation, under the same photocatalytic conditions (pH = 6.5), **Fig. 12-a**. The modified U-Hz1 presented 89% of IC degradation in the 1st cycle, maintaining its high activity up to the 4th cycle (82%). In all reaction cycles, the adsorption percent of IC dye was about 6%. In addition, **Fig. 12-b** shows that the XRD patterns did not change during the photocatalytic reactions. The as-synthesized and recycled U-Hz1 samples presented the (100) and (002) diffraction peaks with similar relative

intensity.

Similarly, **Fig. 12-c** shows the FTIR spectra for the original and recycled U-Hz1 sample, where no significant differences in the bands can be observed. These results indicate that U-Hz1 material presents excellent photostability during the photocatalytic process.

3.9. Discussion

It is common to modify the photocatalytic property of materials to enlarge the visible optical absorption or reduce the bandgap energy [36, 38, 88]. However, more than one property is expected to change when modifiers agents are added to the photocatalytic material. In this case, the in-situ generated NH₃ by the hydrazine decomposition into the synthesis of g-C₃N₄ led to variations in the interplanar stacking structure, the morphology, the C/N ratio (meaning different fractions of N vacancies ate the surface), SA, and optical bandgap, which individually could not explain the differences obtained in the degradation percentage of the IC dye solutions. Therefore, in this work, we evaluate another set of surface properties that have also been reported to play essential roles in the photocatalytic response [24, 89].

In a photocatalytic system, the pH value of the solution is essential. The variation of the pH value has been proposed as a method for selective degradation since the adsorption and degradation of charged pollutants can be controlled by adjusting the surface charge of the photocatalysts. The surface charge of the photocatalyst is modified according to its PZC value. The PZC value or isoelectric point is defined as the pH at which the net surface charge is zero [80]. Generally, when the pH value of the solution is higher than the PZC of the photocatalyst, there is selective adsorption of positively charged pollutants. When pH value is lower than the PZC, negatively charged contaminants are attracted to the surface of the photocatalyst.

However, we did not observe a more pronounced IC adsorption or degradation when pH was selected at 3.5, in which, according to the PZC measured values (PZC > 3.5 for all samples), more anionic IC molecules could be adsorbed on the g-C₃N₄ surface. The PZC increased linearly with the in-situ generated NH₃ content by the hydrazine decomposition (**Fig. 8-b**), but non-linear variation was observed for neither the adsorption capacity at both pH values and the photocatalytic response. The reasons why the PZC value was not correlated with the percentage of degradation might be: (1) there might be some neutral pollutants; (2) the photodegradation of neutral pollutants results in the production of charged species, which will affect the adsorption selectivity of the photocatalysts; and (3) the intermediates are always a mixture of positively charged and negatively charged contaminants [80, 90]. The charged surface inhibits the consecutive degradation of the intermediates with the same charge. However, we could find that the differences in absorption observed at the two pH values follow an exponential trend with the SA, **Fig. 13**.

During the photocatalytic experiments, we did observe a qualitative

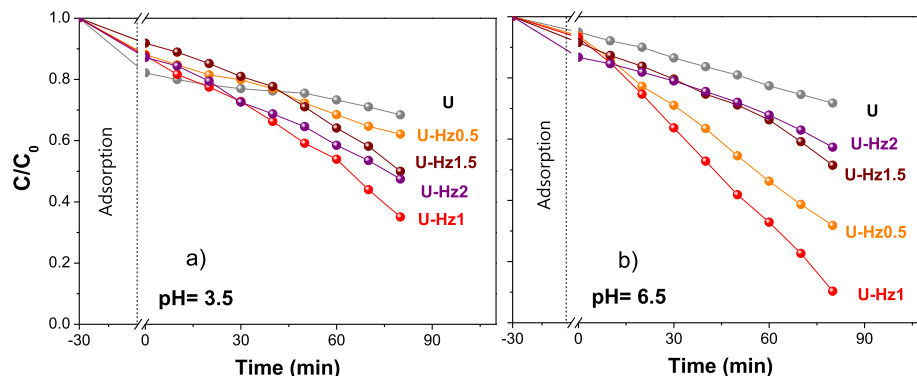


Fig. 10. Plot of C/C_0 of IC dye in solution as a function of blue light irradiation time for the unmodified and modified g-C₃N₄ at pH = a) 3.5 and b) 6.5.

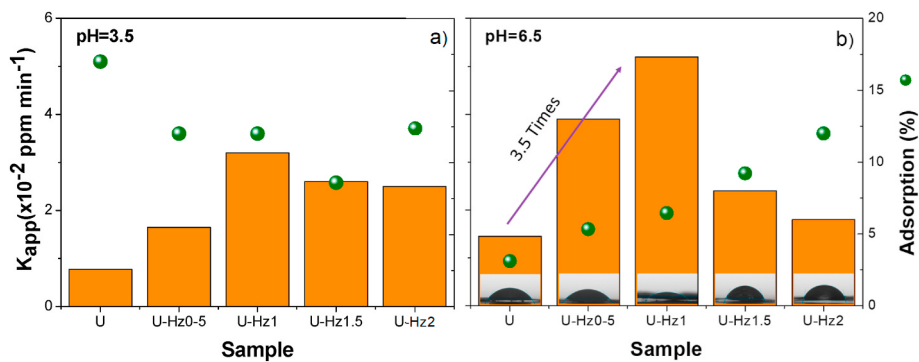


Fig. 11. Adsorption capacity and apparent kinetic rate constant of IC dye photodegradation using unmodified and modified g-C₃N₄ photocatalyst at pH = a) 3.5 and b) 6.5.

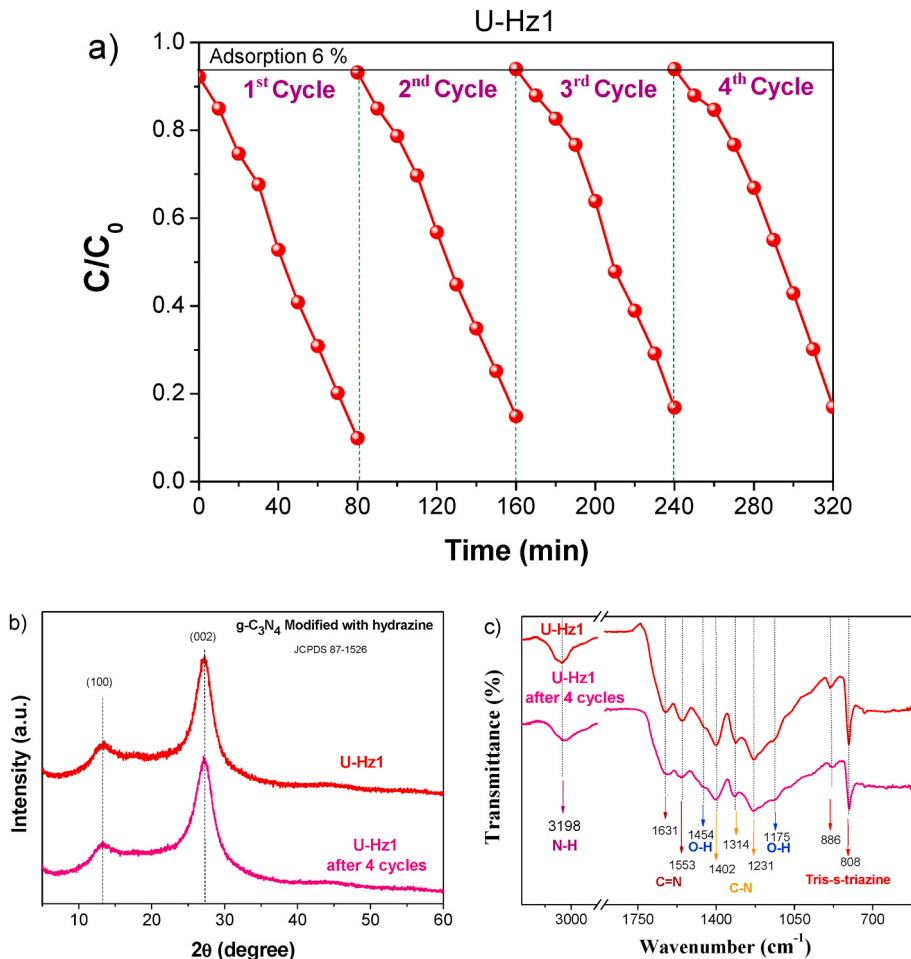


Fig. 12. a) Plot of C/C_0 of IC dye in solution as a function of blue light irradiation time for the U-Hz1 at pH = 6.5 during the 4 cycles, b) X-ray diffraction patterns and c) FTIR analysis of U-Hz1 and recycled U-Hz1 sample after 4th cycle.

difference in the dispersion capacity of the g-C₃N₄ powders in the solution. Thus, the WCA of the samples was measured at pH = 2.7, 4.8, and 6.3. The results indicate that the U-Hz1 has the minimum WCA, i. e. it is the sample with an evident hydrophilic character, also presenting the higher apparent kinetic rate constant at both pHs.

In summary, the addition of hydrazine during the synthesis of g-C₃N₄ led to variations in various structural, morphological, and surface properties. A complex balance between them defines the material with the best photocatalytic response for the degradation of the IC dye. Putting together the different factors that influence the photocatalytic

response, we expected the degradation percentage or apparent kinetic rate constant: (i) to increase with SA, (ii) to increase with the reduction in the optical bandgap, and (iii) to increase with the adsorption capacity measured by the WCA (more surface could be wetted, and therefore more IC molecules could be adsorbed). Fig. 14 shows the plot of the degradation percentage vs. the product SA/(WCA*gap), where it can be seen that for both pHs, the maximum degradation percentage is achieved for the samples with a maximum value of this product (U-Hz1), which provide us a parametric factor to select samples.

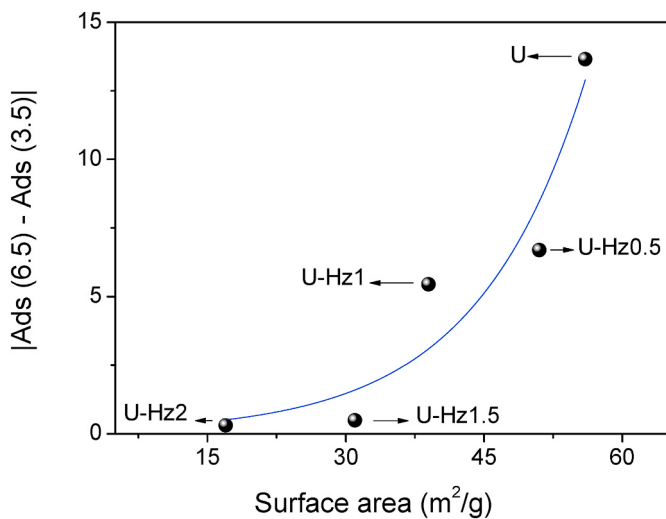


Fig. 13. Plot of differences in absorption at pH = 3.5 and 6.5 vs surface area of unmodified and modified g-C₃N₄ photocatalysts.

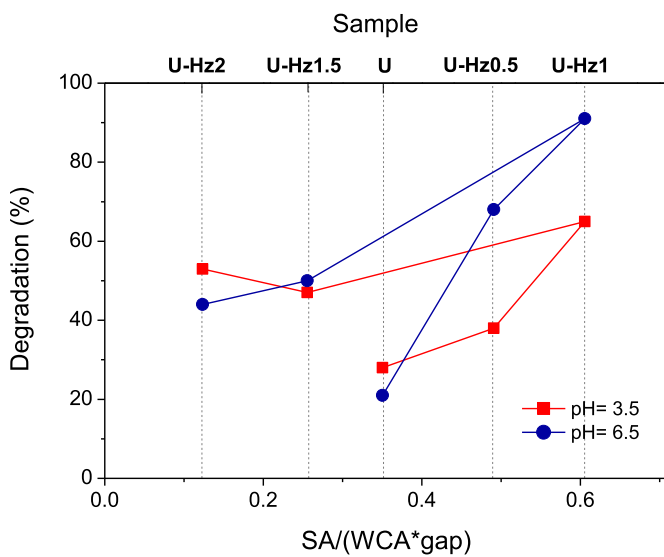


Fig. 14. Plot of the degradation percentage of IC dye vs. the product SA/(WCA*gap) at pH = 3.5 and 6.5 for unmodified and modified g-C₃N₄ photocatalysts.

4. Conclusions

G-C₃N₄ nano-flakes were successfully prepared from urea by heat polymerization, whereas the polymerization in the presence of in-situ generated NH₃ by hydrazine decomposition modifies the interlayer structure, the morphology, the SA, and the surface properties. Increasing the hydrazine content, the g-C₃N₄ increases the interplanar stacking, leading to a more compact structure, exhibiting porous and lamellar plate morphology of low SA. The optical absorption widened towards the visible spectrum leading to clear changes in the color of the samples and probably due to structural defects observed by the increased C/N ratios between 0.71 and 1.1, associated with possible generations of N vacancies suggested by the low PL emission at 2.04 eV. The in-situ generated NH₃ during the polymerization also modified the PZC and WCA values, where the PZC for U-Hz0.5 and U-Hz1 samples were lower than the pristine g-C₃N₄, while for U-Hz1.5 and U-Hz2 attained higher values. Then, the photocatalytic response for the degradation of the IC dye increased following the SA/(WCA*gap) factor, which summarizes

the most important factors. The U-Hz1 sample achieved a 90% IC degradation using blue light at pH = 6.5 in 80 min, which shows long photostability during 4 cycles of reaction.

CRediT authorship contribution statement

Karen Valencia G: Writing – original draft, Visualization, Investigation, Data curation. **Agileo Hernández-Gordillo:** Writing – review & editing, Methodology, Conceptualization. **Melissa Méndez-Galván:** Formal analysis. **Diego Morett:** Formal analysis. **Sandra E. Rodil:** Writing – review & editing, Conceptualization.

Declaration of competing interest

The authors declare that they have no known competing financial interests or personal relationships that could have appeared to influence the work reported in this paper.

Data availability

No data was used for the research described in the article.

Acknowledgments

Karen Valencia thanks CONACYT México for PhD scholarship. The authors thank to CONACYT for the Catedras-Conacyt/1169 and financial support from CONACYT (Grant No. 1740 y CB-A1-S-8729). Finally, the authors recognized the support of Adriana Tejeda, Lourdes Bazán Díaz, Phaedra S. Silva, Alejandro Pompa, Diego Solis, and M. Angel Canseco for making possible the different measurements.

Appendix A. Supplementary data

Supplementary data to this article can be found online at <https://doi.org/10.1016/j.mssp.2022.106900>.

References

- [1] M. N, V. S, Keerthi, A novel g-C₃N₄/MnV₂O₆ heterojunction photocatalyst for the removal of methylene blue and indigo carmine, *Chem. Phys. Lett.* (2019) 737.
- [2] Y. Sun, et al., Facile synthesis of free-metal ternary composites for ultra-fast photocatalytic degradation of organic pollutant, *Catal. Today* 340 (2020) 294–301.
- [3] R.M.F. Bento, et al., Improvements in the enzymatic degradation of textile dyes using ionic-liquid-based surfactants, *Separ. Purif. Technol.* (2020) 235.
- [4] S.K. Ray, D. Dhakal, S.W. Lee, Visible light driven Ni-BaMo₃O₁₀ photocatalyst for Indigo Carmine degradation: Mechanism and pathways, *Mater. Sci. Semicond. Process.* (2020) 105.
- [5] A. Hernández-Gordillo, et al., Photodegradation of Indigo Carmine dye by CdS nanostructures under blue-light irradiation emitted by LEDs, *Catal. Today* 266 (2016) 27–35.
- [6] K.T.C. Qinglin Zhang, Adsorption of organic pollutants from effluents of a kraft pulp mill on activated carbon and polymer resin, *Adv. Environ. Res.* 3 (2001) 8.
- [7] Y.J. Chan, et al., A review on anaerobic-aerobic treatment of industrial and municipal wastewater, *Chem. Eng. J.* 155 (1–2) (2009) 1–18.
- [8] F.P. van der Zee, S. Villaverde, Combined anaerobic-aerobic treatment of azo dyes— a short review of bioreactor studies, *Water Res.* 39 (8) (2005) 1425–1440.
- [9] M. Luo, et al., Supported growth of inorganic-organic nanoflowers on 3D hierarchically porous nanofibrous membrane for enhanced enzymatic water treatment, *J. Hazard Mater.* 381 (2020), 120947.
- [10] A.I. Navarro-Aguilar, et al., An efficient and stable WO₃/g-C₃N₄ photocatalyst for ciprofloxacin and orange G degradation, *J. Photochem. Photobiol. Chem.* (2019) 384.
- [11] K.R.S. Devi, et al., Biogenic synthesis of g-C₃N₄/Bi₂O₃ heterojunction with enhanced photocatalytic activity and statistical optimization of reaction parameters, *Appl. Surf. Sci.* 494 (2019) 465–476.
- [12] G. Pirgholi-Givi, S. Farjam-Shayesteh, Y. Azizian-Kalandaragh, The influence of preparation parameters on the photocatalytic performance of mixed bismuth titanate-based nanostructures, *Phys. B Condens. Matter* (2019) 575.
- [13] L. Nasi, et al., ZnS and ZnO Nanosheets from ZnS(en)0.5 Precursor: nanoscale Structure and Photocatalytic Properties, *J. Phys. Chem. C* 116 (12) (2012) 6960–6965.
- [14] Y. Li, et al., Rapid fabrication of SnO₂ nanoparticle photocatalyst: computational understanding and photocatalytic degradation of organic dye, *Inorg. Chem. Front.* 5 (12) (2018) 3005–3014.

- [15] G. Nagaraju, et al., Photocatalytic activity of ZnO nanoparticles: synthesis via solution combustion method, *Mater. Today Proc.* 4 (11) (2017) 11700–11705.
- [16] Y. Cui, et al., Fabrication of Dual Z-Scheme MIL-53(Fe)/ α -Bi₂O₃/g-C₃N₄ Ternary Composite with Enhanced Visible Light Photocatalytic Performance, Separation and Purification Technology, 2020, p. 232.
- [17] F. Liu, et al., Construction of Z-Scheme -C₃N₄/Ag/P₃HT Heterojunction for Enhanced Visible-Light Photocatalytic Degradation of Tetracycline (TC) and Methyl Orange (MO), *Applied Surface Science*, 2019, p. 496.
- [18] Z. Feng, et al., In situ preparation of g-C₃N₄/Bi₄O₅I₂ complex and its elevated photoactivity in Methyl Orange degradation under visible light, *J. Environ. Sci. (China)* 87 (2020) 149–162.
- [19] X. Zhao, et al., Ag supported Z-scheme WO_{2.9}/g-C₃N₄ composite photocatalyst for photocatalytic degradation under visible light, *Appl. Surf. Sci.* (2020) 501.
- [20] Q. Zhang, et al., Facile fabrication of novel Ag₂S/K-g-C₃N₄ composite and its enhanced performance in photocatalytic H₂ evolution, *J. Colloid Interface Sci.* 568 (2020) 117–129.
- [21] D. Ayodhya, G. Veerabhadram, Synthesis and characterization of g-C₃N₄ nanosheets decorated Ag₂S composites for investigation of catalytic reduction of 4-nitrophenol, antioxidant and antimicrobial activities, *J. Mol. Struct.* 1186 (2019) 423–433.
- [22] S. Velmurugan, et al., Synthesis of novel and environmental sustainable AgI-Ag₂S nanospheres impregnated g-C₃N₄ photocatalyst for efficient degradation of aqueous pollutants, *Appl. Surf. Sci.* (2020) 500.
- [23] L. Meng, et al., Photocatalytic behavior of biochar-modified carbon nitride with enriched visible-light reactivity, *Chemosphere* 239 (2020), 124713.
- [24] D.B. Hernández-Uresti, et al., Performance of the polymeric g-C₃N₄ photocatalyst through the degradation of pharmaceutical pollutants under UV-vis irradiation, *J. Photochem. Photobiol. Chem.* 324 (2016) 47–52.
- [25] C. Hu, et al., Simple synthesis of 3D flower-like g-C₃N₄/TiO₂ composite microspheres for enhanced visible-light photocatalytic activity, *J. Mater. Sci.* 55 (1) (2019) 151–162.
- [26] I. Papailias, et al., Effect of processing temperature on structure and photocatalytic properties of g-C₃N₄, *Appl. Surf. Sci.* 358 (2015) 278–286.
- [27] Y. Chen, et al., Surface modification of g-C₃N₄ by hydrazine: Simple way for noble-metal free hydrogen evolution catalysts, *Chem. Eng. J.* 286 (2016) 339–346.
- [28] A. Mohammad, et al., Synergistically Effective and Highly Visible Light Responsive SnO₂-C₃N₄ Nanostructures for Improved Photocatalytic and Photoelectrochemical Performance, *Applied Surface Science*, 2019, p. 495.
- [29] H. Dong, et al., Synthesis of g-C₃N₄ by different precursors under burning explosion effect and its photocatalytic degradation for tylosin, *Appl. Catal. B Environ.* 230 (2018) 65–76.
- [30] F. Dong, et al., In situ construction of g-C₃N₄/g-C₃N₄ metal-free heterojunction for enhanced visible-light photocatalysis, *ACS Appl. Mater. Interfaces* 5 (21) (2013) 11392–11401.
- [31] W. Zhang, et al., Hydrazone-linked heptazine polymeric carbon nitrides for synergistic visible-light-driven catalysis, *Chemistry* 26 (33) (2020) 7358–7364.
- [32] B. Palanivel, et al., Magnetic binary metal oxide intercalated g-C₃N₄: Energy band tuned p-n heterojunction towards Z-scheme photo-Fenton phenol reduction and mixed dye degradation, *J. Water Proc. Eng.* (2019) 32.
- [33] X.-F. Song, et al., Novel in-situ radiation construction of thioglycollic acid capped CdS quantum dots functionalized g-C₃N₄ nano-hybrids with superior photocatalytic activity under visible light, *Radiat. Phys. Chem.* (2019) 165.
- [34] S. Kumar, V.R. Battula, K. Kailasam, Single molecular precursors for C_xN_y materials- Blending of carbon and nitrogen beyond g-C₃N₄, *Carbon* 183 (2021) 332–354.
- [35] M. Soto-Herranz, et al., Effects of protonation, hydroxylamination, and hydrazination of g-C(3)N(4) on the performance of matrimid(R)/g-C(3)N(4) membranes, *Nanomaterials* 8 (12) (2018).
- [36] L. Kong, et al., Porous size dependent g-C₃N₄ for efficient photocatalysts: Regulation synthesizes and physical mechanism, *Mater. Today Energy* 13 (2019) 11–21.
- [37] S. Zhang, et al., Enhanced photodegradation of toxic organic pollutants using dual-oxygen-doped porous g-C₃N₄: Mechanism exploration from both experimental and DFT studies, *Appl. Catal. B Environ.* 248 (2019) 1–10.
- [38] L. Kong, et al., Site-selected N vacancy of g-C₃N₄ for photocatalysis and physical mechanism, *Appl. Mater. Today* 13 (2018) 329–338.
- [39] J. Fang, et al., Nitrogen self-doped graphitic carbon nitride as efficient visible light photocatalyst for hydrogen evolution, *J. Mater. Chem. 3* (26) (2015) 13819–13826.
- [40] L. Shi, et al., Photoassisted Construction of holey Defective g-C₃N₄ Photocatalysts for efficient visible-light-driven H₂ O₂ production, *Small* (9) (2018) 14.
- [41] X. Wu, et al., Soluble g-C₃N₄ nanosheets: Facile synthesis and application in photocatalytic hydrogen evolution, *Appl. Catal. B Environ.* 247 (2019) 70–77.
- [42] X. Du, et al., A scalable chemical route to soluble acidified graphitic carbon nitride: an ideal precursor for isolated ultrathin g-C₃N₄ nanosheets, *Nanoscale* 7 (19) (2015) 8701–8706.
- [43] A.R. Muhammad Farooq, The Determination of Point Zero Charge (PZC) of Al₂O₃-MgO Mixed Oxides, 19–29 sep, National Postgraduate Conference, 2011, p. 5.
- [44] B.M. Babic, S.K. M, M.J. Polovina, B. V, Kaludierovic Point of zero charge and intrinsic equilibrium constants of activated carbon cloth, *Carbon* 37 (1999) 5.
- [45] S. Sood, et al., α -Bi₂O₃ nanorods: An efficient sunlight active photocatalyst for degradation of Rhodamine B and 2,4,6-trichlorophenol, *Ceram. Int.* 41 (3) (2015) 3355–3364.
- [46] S. Huang, Y. Zhao, R. Tang, Facile fabrication of a Cu@g-C₃N₄ nanocatalyst and its application for the aerobic oxidations of alkylaromatics and the reduction of 4-nitrophenol, *RSC Adv.* 6 (93) (2016) 90887–90896.
- [47] N. Meng, et al., Engineering oxygen-containing and amino groups into two-dimensional atomically-thin porous polymeric carbon nitrogen for enhanced photocatalytic hydrogen production, *Energy Environ. Sci.* 11 (3) (2018) 566–571.
- [48] K. Zhong, et al., Fabrication of BiVO₄@g-C₃N₄(100) heterojunction with enhanced photocatalytic visible-light-driven activity, *J. Solid State Chem.* 274 (2019) 142–151.
- [49] R. Tejasvi, S. Basu, Formation of C₃N₄ thin films through the stoichiometric transfer of the bulk synthesized g-C₃N₄ using RFM sputtering, *Vacuum* (2020) 171.
- [50] R. Kumar, M.A. Barakat, F.A. Alseroury, Oxidized g-C₃N₄/polyaniline nanofiber composite for the selective removal of hexavalent chromium, *Sci. Rep.* 7 (1) (2017), 12850.
- [51] C. Fan, et al., Graphitic carbon nitride nanosheets obtained by liquid stripping as efficient photocatalysts under visible light, *RSC Adv.* 7 (59) (2017) 37185–37193.
- [52] Y. Kang, et al., An amorphous carbon nitride photocatalyst with greatly extended visible-light-responsive range for photocatalytic hydrogen generation, *Adv. Mater.* 27 (31) (2015) 4572–4577.
- [53] Z. Huang, et al., Constructing g-C₃N₄ quantum dots modified g-C₃N₄/GO nanosheet aerogel for UV-Vis-NIR driven highly efficient photocatalytic H₂ production, *Int. J. Hydrogen Energy* 44 (59) (2019) 31041–31052.
- [54] G. Picho-Chillán, et al., Photodegradation of Direct Blue 1 azo dye by polymeric carbon nitride irradiated with accelerated electrons, *Mater. Chem. Phys.* (2019) 237.
- [55] C. Prasad, H. Tang, I. Bahadur, Graphitic carbon nitride based ternary nanocomposites: from synthesis to their applications in photocatalysis: a recent review, *J. Mol. Liq.* 281 (2019) 634–654.
- [56] H. Xiao, et al., Photocatalytic performances of g-C₃N₄ based catalysts for RhB degradation: Effect of preparation conditions, *Appl. Surf. Sci.* 358 (2015) 313–318.
- [57] P.J. Askey, The thermal decomposition of hydrazine, *Elgin and Taylor* 52 (1930) 5.
- [58] Process for Preparing Hydrazodicarbonamide, European Patent, 1985, 0163526.
- [59] H. Chen, et al., SNCR De-NO_x within a moderate temperature range using urea-spiked hydrazine hydrate as reductant, *Chemosphere* 161 (2016) 208–218.
- [60] S. Wang, et al., Controllable synthesis of nanotube-type graphitic C₃N₄ and their visible-light photocatalytic and fluorescent properties, *J. Mater. Chem. 2* (9) (2014).
- [61] P. Cendula, et al., Directional roll-up of nanomembranes mediated by wrinkling, *Nano Lett.* 11 (1) (2011) 236–240.
- [62] W. An, et al., The Z-scheme Ag₂CO₃@g-C₃N₄ core-shell structure for increased photoinduced charge separation and stable photocatalytic degradation, *Appl. Surf. Sci.* (2020) 504.
- [63] Q. Zhang, et al., A photocatalytic degradation strategy of PPCPs by a heptazine-based CN organic polymer (OCN) under visible light, *Environ. Sci. J. Integr. Environ. Res.: Nano* 5 (10) (2018) 2325–2336.
- [64] Z. Mao, et al., Modification of surface properties and enhancement of photocatalytic performance for g-C₃N₄ via plasma treatment, *Carbon* 123 (2017) 651–659.
- [65] F. Chang, et al., Heterojuncted non-metal binary composites silicon carbide/g-C₃N₄ with enhanced photocatalytic performance, *Mater. Sci. Semicond. Process.* 75 (2018) 183–192.
- [66] H. Medetalibeyoglu, An investigation on development of a molecular imprinted sensor with graphitic carbon nitride (g-C₃N₄) quantum dots for detection of acetaminophen, *Carbon Lett.* 31 (6) (2021) 1237–1248.
- [67] S. Ghobane, et al., Comparison of the XPS spectra from homoepitaxial {111}, {100} and polycrystalline boron-doped diamond films, *Diam. Relat. Mater.* 19 (5–6) (2010) 630–636.
- [68] D. Wang, et al., In-situ growth of β -Bi₂O₃ nanosheets on g-C₃N₄ to construct direct Z-scheme heterojunction with enhanced photocatalytic activities, *J. Alloys Compd.* (2021) 859.
- [69] A.P. Dementjev, et al., X-Ray photoelectron spectroscopy reference data for identification of the C N phase in carbon]nitrogen films, *Diam. Relat. Mater.* 9 (2000) 4.
- [70] P. Martín-Ramos, et al., A simple approach to synthesize g-C₃N₄ with high visible light photoactivity for hydrogen production, *Int. J. Hydrogen Energy* 40 (23) (2015) 7273–7281.
- [71] A.P. Dementjev, et al., X-Ray Photoelectron Spectroscopy reference data for identification of the C₃N₄ phase in carbon-nitrogen films.pdf, *Diam. Relat. Mater.* 9 (2000) 4.
- [72] H. Zhang, et al., Improved H₂O₂ Photogeneration by KOH-Doped -C₃N₄ under Visible Light Irradiation Due to Synergistic Effect of N Defects and K Modification, *Applied Surface Science*, 2020, p. 527.
- [73] B. Choudhury, et al., Evolution of nitrogen-related defects in graphitic carbon nitride nanosheets probed by positron annihilation and photoluminescence spectroscopy, *J. Phys. Chem. C* 122 (16) (2018) 9209–9219.
- [74] D. Das, et al., Defect induced tuning of photoluminescence property in graphitic carbon nitride nanosheets through synthesis conditions, *J. Lumin.* 185 (2017) 155–165.
- [75] A. Ghosh, et al., Nitrogen vacancy and hydrogen substitution mediated tunable optoelectronic properties of g-C₃N₄ 2D layered structures: Applications towards blue LED to broad-band photodetection, *Appl. Surf. Sci.* (2021) 556.
- [76] D. Ruan, et al., Defects rich g-C₃N₄ with mesoporous structure for efficient photocatalytic H₂ production under visible light irradiation, *Appl. Catal. B Environ.* 238 (2018) 638–646.
- [77] W. Zhou, et al., Metal-free Hydrophilic D-A Conjugated Polyelectrolyte Dots/-C₃N₄ Nanosheets Heterojunction for Efficient and Irradiation-Stable Water-Splitting Photocatalysis, *Applied Catalysis B: Environmental*, 2020, p. 270.
- [78] G. Dong, Z. Ai, L. Zhang, Efficient anoxic pollutant removal with oxygen functionalized graphitic carbon nitride under visible light, *RSC Adv.* 4 (11) (2014).

- [79] F. Jia, et al., In-situ Construction of Superhydrophilic g-C₃N₄ Film by vapor-assisted confined Deposition for photocatalysis, *Fron. Mater.* (2019) 6.
- [80] H.A. Ghaly, et al., Stable plasmonic Ag/AgCl–polyaniline photoactive composite for degradation of organic contaminants under solar light, *RSC Adv.* 7 (21) (2017) 12726–12736.
- [81] P.-S. Konstas, et al., Synthesis, Characterization of g-C₃N₄/SrTiO₃ Heterojunctions and photocatalytic Activity for organic pollutants degradation, *Catalysts* 8 (11) (2018).
- [82] A. Hernández-Gordillo, et al., Photocatalytic activity of enlarged microrods of α-Bi₂O₃ produced using ethylenediamine-solvent, *Ceram. Int.* 42 (10) (2016) 11866–11875.
- [83] B. Zhu, et al., Isoelectric point and adsorption activity of porous g-C₃N₄, *Appl. Surf. Sci.* 344 (2015) 188–195.
- [84] A. Hernández-Gordillo, et al., Good practices for reporting the photocatalytic evaluation of a visible-light active semiconductor: Bi₂O₃, a case study, *Catal. Sci. Technol.* 9 (6) (2019) 1476–1496.
- [85] A.J. Kettle, B.M. Clark, C.C. Winterbourn, Superoxide converts indigo carmine to isatin sulfonic acid: implications for the hypothesis that neutrophils produce ozone, *J. Biol. Chem.* 279 (18) (2004) 18521–18525.
- [86] C.M. Antonio-Cisneros, et al., TiO₂ immobilized on Manihot carbon: optimal preparation and evaluation of its activity in the decomposition of indigo carmine, *Int. J. Mol. Sci.* 16 (1) (2015) 1590–1612.
- [87] T.T. Guaraldo, et al., On the application of nanostructured electrodes prepared by Ti/TiO₂/WO₃ "template": a case study of removing toxicity of indigo using visible irradiation, *Chemosphere* 91 (5) (2013) 586–593.
- [88] L. Kong, et al., Graphitic carbon nitride nanostructures: Catalysis, *Appl. Mater. Today* 16 (2019) 388–424.
- [89] Z. Abbasi, et al., Superparamagnetic recoverable flowerlike Fe₃O₄@Bi₂O₃ core–shell with g-C₃N₄ sheet nanocomposite: synthesis, characterization, mechanism and kinetic study of photo-catalytic activity, *J. Mater. Sci. Mater. Electron.* 31 (2) (2019) 1022–1033.
- [90] M. Fronczak, et al., Extraordinary adsorption of methyl blue onto sodium-doped graphitic carbon nitride, *J. Phys. Chem. C* 121 (29) (2017) 15756–15766.